Joint Equivalence Design and Analysis of a Tensegrity Joint

Bingxing Chen
School of Mechatronics Engineering,
Harbin Institute of Technology,
Harbin, Heilongjiang Province 150001, China
e-mail: bingxingchen@yeah.net

Hongzhou Jiang[1]
School of Mechatronics Engineering,
Harbin Institute of Technology,
Harbin, Heilongjiang Province 150001, China
e-mail: jianghz@hit.edu.cn

Jingxuan Liu
School of Mechatronics Engineering,
Harbin Institute of Technology,
Harbin, Heilongjiang Province 150001, China
e-mail: 1054454590@qq.com

Shuaibo Lu
School of Mechatronics Engineering,
Harbin Institute of Technology Harbin,
Heilongjiang Province 150001, China
e-mail: 20S008040@stu.hit.edu.cn

We propose a method to design a tensegrity joint, making its elastic deformation an accurate joint-like motion, such as a rotation around the designed rotational center. The tensegrity joint can be a revolute, universal, and ball joint through this method. Axis drift is presented as a design criterion to describe the rotational center's deviation degree with respect to the compliance center since the rotational center is not fixed to one point for different positions of the tensegrity joint. The axis drift is designed to be in a prescribed range so that the tensegrity joint is approximately equivalent to a rigid joint. In other words, the tensegrity joint's elastic response under external torque and force becomes precise rigid joint-like kinematics and can replace rigid joints to transfer motion, force, and energy. A large-size tensegrity rotational joint is developed to verify the joint equivalence experimentally. The experimental results show that the tensegrity joint achieved maximum dimensionless axis drift of less than 2%, which indicates an excellent joint equivalence. The tensegrity joints' ability to replace rigid joints as modular joints to construct a hyper redundant serial structure is demonstrated using a tensegrity robotic arm. The proposed compliant tensegrity joint has notable benefits of tensegrity structure, such as high mechanical efficiency, modularity, and scalability. It can be extended to many robotic applications, such as large-size serial robotic arms and snake-like robots. [DOI: 10.1115/1.4051106]

Keywords: tensegrity joint, compliant mechanisms, mechanism design, parallel platforms, soft robots

1 Introduction

Tensegrity systems are composed of compression elements and tension elements and kept in a self-stressed equilibrium state by their compliant tension network [1,2]. Tensegrities are emerging as the future structural systems [3] and are notable for many exciting and beneficially features such as high efficiency, redundant, stiffness adjustability, impressive strength-to-weight ratio, strong environment adaptability, modularity, and scalability [1–3]. For example, they are demonstrated at different scales in the world, ranging from the mechanical structures in living cells [4] to the applications in bridges [5] and domes [6]. Tensegrity structures blossom in applied areas of art, architecture, civil engineering, and biology [4–8] and nowadays have been permeating into robotics [2]. Research has been performed to adopt tensegrity structures to design various robots [9–12], such as NASA's super ball for space exploration [13], duct climbing tensegrity robots [14], and tensegrity swimmers [15,16].

Tensegrity joints are essential components of tensegrity structures. They have been previously implemented in human limbs and vertebrae from biological aspects, such as Felmon's tensegrity saddle joint and Levin's wire-spoken wheel model [17–20]. In these biological systems, tensegrity joints play a crucial role in achieving a wide range of motion and structural compliance. Unlike conventional rigid joints (ball type, roller type, and linkage type), such compliant tensegrity joints [21–24] have unique physical properties that make them ideal for interaction with uncertain or unpredictable environments and are more friendly to interact with a human.

In our previous paper [16], we presented a one degree-of-freedom (DOF) tensegrity rotational joint and assembled six tensegrity joints to construct a vibration-driven robotic fish. We focused on the joint's passive properties and briefly introduced its design principle and joint equivalence that a tensegrity joint is equivalent to a rigid rotational joint. Such equivalence is confirmed since the compliance center is approximately the virtual rotational center of our tensegrity joint at the neutral pose based on its stiffness matrix [16]. It is necessary and significant to propose a design criterion to describe the joint equivalence during motion.

For compliant joints, the index of axis drift is often used to describe joint equivalence, which indicates the accuracy of joint-like motions, rotation around one center, or translation along one axis, comparing to conventional rigid joints. It has been used as an essential design criterion of flexure hinges to achieve highly precise positioning and contributes a lot to their successful applications in micro/nano systems [25–28]. Similarly, we would also regard the axis drift as a design criterion to help design our tensegrity joints.

This article implements the tensegrity rotational joint's design criterion in the designing process and develops a large-size and multi-DOF tensegrity rotational joint. Section 2 introduces the structure of the tensegrity joint and formulates its stiffness. In Sec. 3, the joint's design method is introduced, including the decoupling, anisotropy design of its stiffness, and joint equivalence analysis. The axis drift is proposed to evaluate the joint equivalence of the tensegrity joints. Numerical examples are presented to elaborate on the joint equivalence and to verify the proposed design method's effectiveness. Section 4 proposes two experiments. In the first experiment, the axis drifts of a 3-DOF tensegrity rotational joint are measured to demonstrate the joint equivalence. The second experiment shows the application of the tensegrity joint constructing a robotic arm. Significance, future works, and expanded applications of the proposed tensegrity joint are discussed. Finally, the conclusions are summarized.

2 Structure and Stiffness

2.1 Structure of a Tensegrity Joint. Generally, tensegrity structures are composed of two main components: compression elements and tension elements. The compression elements are not limited to being the axially loaded members (bars and struts) and also can be various rigid bodies [16,29,30], such as curved compressed members [30]. The tensegrity structure with rigid bodies as general compression members is referred to herein as general
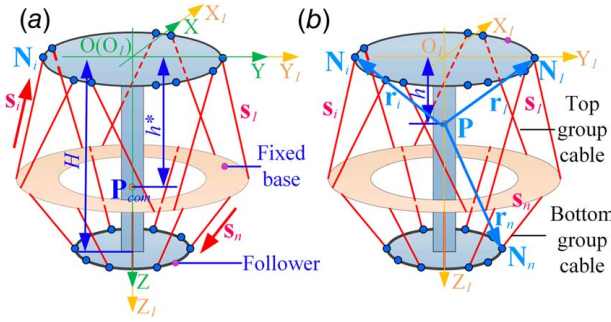
Fig. 1 A general model of a tensegrity joint

tensegrity. The generality of compression elements also can be seen from the various bones as compressed members in the emerging bio-tensegrity models [7,17,19].

A general model of a tensegrity joint is shown in Fig. 1. The tensegrity joint's compression elements are two platforms, a base, and a follower. The joint keeps a self-stressed equilibrium state by its compliant tension network composed of n cables at the neutral pose (zero translations and rotations). Vectors $\mathbf{s}_1, \ldots, \mathbf{s}_i, \ldots, \mathbf{s}_n$ are vectors along the cables pointing toward the follower from the fixed base, and their anchor points on the follower are $\mathbf{N}_1, \ldots, \mathbf{N}_i,$ $\ldots, \mathbf{N}_n$ in Fig. 1(b). To describe the follower's motion, we define the base frame, B: O-XYZ, and the body frame, M: O_1-$X_1Y_1Z_1$, for the base and follower. There is an arbitrary point $\mathbf{P}$ on the z-axis described by $\mathbf{P} = [0 \quad 0 \quad h]^T$, where h is its z coordinate in the body frame. Vectors $\mathbf{r}_1, \ldots, \mathbf{r}_i, \ldots, \mathbf{r}_n$ are the position vectors of cables" anchor points on the follower with respect to the point $\mathbf{P}$ in Fig. 1(b).

In general, all the cables in the tensegrity model can be individually designed. However, it would increase design complexity due to the massive number of individual design cable parameters. Inspired by cable arrangements in the Stewart–Gough parallel mechanism [31], the tensegrity joints' cable network is regular to simplify its design. The cables can be divided into two groups: the bottom and top groups in Fig. 1. The cables in each group can be generated from one cable, such as the first cable or nth cable, using reflective and rotational operations.

Here, we mainly focus on the elastic response of the proposed tensegrity joint under external load or workload. The elastic deformation of the proposed tensegrity joint in Fig. 1 would be a rotation around an approximately fixed point through the proposed design method. Before proposing the design method, the tensegrity joint's stiffness is introduced first, reflecting the elastic deformation of elastic systems.

2.2 Stiffness of a Tensegrity Joint. According to the works proposed by Behzadipour et al. [32], the stiffness of the tensegrity joints at the point $\mathbf{P}$ is written as follows:

$$\mathbf{K} = \sum_{i=1}^n \left(k_i - \frac{\tau_i}{l_i} \right) \mathbf{J}_i^T \mathbf{J}_i + \sum_{i=1}^n \frac{\tau_i}{l_i} \begin{bmatrix} \mathbf{I} & (\mathbf{r}_i^\times)^T \\ \mathbf{r}_i^\times & \mathbf{r}_i^\times(\mathbf{r}_i^\times)^T \end{bmatrix} - \sum_{i=1}^n \tau_i \begin{bmatrix} \mathbf{0} & \mathbf{0} \\ \mathbf{0} & \mathbf{s}_{ni}^\times \mathbf{r}_i^\times \end{bmatrix}$$
(1)

where k_i, τ_i, and l_i represent the stiffness, elastic force, and length of the ith cable, respectively, and $\mathbf{s}_{ni}$ represents the unit vector along the ith cable. The term $\mathbf{r}_i^\times$ is the antisymmetric matrix of the vector $\mathbf{r}_i$ and the matrix operator of the cross product.

The Jacobian matrix $\mathbf{J}$ mapping the coordinate variation of the joint, $d\mathbf{p}$, to the length variation of the cables, $d\mathbf{l}$, is written as follows:

$$\mathbf{J} = \frac{d\mathbf{l}}{d\mathbf{p}} = \begin{bmatrix} \mathbf{J}_1 & \cdots & \mathbf{J}_n \end{bmatrix}^T$$
(2)

where its component $\mathbf{J}_i$ of the ith cable is defined as $\mathbf{J}_i = \begin{bmatrix} \mathbf{s}_{ni}^T & (\mathbf{r}_i^\times \mathbf{s}_{ni})^T \end{bmatrix}^T$.

Substituting Eq. (2) into Eq. (1), the stiffness is rewritten as follows:

$$\mathbf{K} = \begin{bmatrix} \mathbf{K}_{Tran} & \mathbf{K}_{CP}^T \\ \mathbf{K}_{CP} & \mathbf{K}_{Rot} \end{bmatrix}$$
(3)

where $\mathbf{K}_{Tran} = \sum_{i=1}^n \mathbf{K}_{Ti}$ is the translational stiffness of the tensegrity joint, where $\mathbf{K}_{Ti} = k_i \mathbf{s}_{ni} \mathbf{s}_{ni}^T + \frac{\tau_i}{l_i}(\mathbf{I}_3 - \mathbf{s}_{ni}\mathbf{s}_{ni}^T)$ is a symmetric stiffness. The stiffness $\mathbf{K}_{CP} = \sum_{i=1}^n \mathbf{r}_i \times \mathbf{K}_{Ti}$ is the coupling stiffness of the joint, and $\mathbf{K}_{Rot} = \sum_{i=1}^n \mathbf{r}_i^\times \mathbf{K}_{Ti}(\mathbf{r}_i^\times)^T - \sum_{i=1}^n \tau_i \mathbf{s}_{ni}^\times \mathbf{r}_i^\times$ is the rotational stiffness of the joint.

Observing $\mathbf{r}_i = \mathbf{N}_i - \mathbf{P}$, the antisymmetric matrix $\mathbf{r}_i^\times$ is rewritten as follows:

$$\mathbf{r}_i^\times = \mathbf{N}_i^\times - \mathbf{P}^\times$$
(4)

Since $\mathbf{P}$ is independent of cables, the coupling stiffness is rewritten as follows:

$$\mathbf{K}_{CP} = \sum_{i=1}^n (\mathbf{N}_i^\times - \mathbf{P}^\times)\mathbf{K}_{Ti} = \mathbf{K}_{Tu} - \mathbf{P}^\times \mathbf{K}_{Tran}$$
(5)

where $\mathbf{K}_{Tu} = \sum_{i=1}^n \mathbf{N}_i^\times \mathbf{K}_{Ti}$.

3 Design Method

3.1 Design Principle. The tensegrity joint in Fig. 1 is a multi-DOF mass–spring system composed of elastic tension elements. Its essential characteristic is the stiffness along different directions, such as translations and rotations (x, y, z, ϕ, θ, and ψ). Along the direction of low stiffness, the joint's capability to resist external load is weaker than in the direction of high stiffness. In other words, the joint along the direction of low stiffness would have a higher degree-of-freedom than along the direction of high stiffness. Therefore, low stiffness can be considered one pseudo-DOF for the proposed tensegrity joints, and high stiffness can be regarded as constraints. Furthermore, zero stiffness along one direction means totally free along this direction. Infinitely high stiffness indicates strong constraints. For example, a rigid rotational joint's rotational stiffness is lower than its translational stiffness and is often approximately zero.

The relationship between the stiffness anisotropy and DOFs is the primary design principle to make the proposed tensegrity joint achieve precise rigid joint-like kinematics. There are three steps to design the tensegrity joint. Decoupling the stiffness is the first step to lay the foundation for designing each DOF's stiffness independently from determining the tensegrity joint's virtual rotational center. The stiffness anisotropy design is the second step. After giving the required DOFs, the stiffness anisotropy should be achieved to design the joint. The two steps are completed at the neutral pose to obtain an analytical solution about the stiffness. In the third step, the joint equivalence of the tensegrity joint is analyzed at other positions.

The tensegrity joint can be designed to be a revolute joint, universal joint, and ball joint around a specific rotational center through the design method. We will detail the three steps and their significance.

3.2 Stiffness Decoupling and the Compliance Center. Since the tensegrity joint in Fig. 1 adopts the regular arrangements of tension elements, its stiffness matrix in Eq. (3) at the neutral pose is written as follows [33]:

$$\mathbf{K} = \begin{bmatrix} K_x & 0 & 0 & 0 & K_{x\theta} & 0 \\ 0 & K_y & 0 & K_{y\phi} & 0 & 0 \\ 0 & 0 & K_z & 0 & 0 & 0 \\ 0 & K_{y\phi} & 0 & K_\phi & 0 & 0 \\ K_{x\theta} & 0 & 0 & 0 & K_\theta & 0 \\ 0 & 0 & 0 & 0 & 0 & K_\psi \end{bmatrix}$$
(6)

where K_p represents the stiffness along p direction, and K_{pq} represents the coupling stiffness of the p direction and the q direction, where the subscripts p and q are the directions such as x, y, z, ϕ, θ, and ψ.

The stiffness in Eq. (6) should be decoupled so that each DOF's stiffness can be designed independently. From the mathematical aspect, the decoupling implies that the direction of the stiffness matrix's independent eigenvectors can be designed to be consistent with the corresponding DOF in the Cartesian coordinate. The tensegrity joint is fully decoupled if $\mathbf{K}_{CP} = \mathbf{0}_{3 \times 3}$, that is, $K_{y\phi} = K_{x\theta} = 0$. The decoupling condition is rewritten as follows:

$$\mathbf{K}_{CP} = \mathbf{0}_{3 \times 3} \Rightarrow \mathbf{P}_{com}^{\times} = \mathbf{P}^{\times}|_{\mathbf{K}_{CP} = \mathbf{0}_{3 \times 3}} = \mathbf{K}_{Tu} \mathbf{K}_{Tran}^{-1} \quad (7)$$

When $\mathbf{P} = \mathbf{P}_{com}$, this point is the compliance center [16,33] at which six DOFs are decoupled. The compliance center is described by $\mathbf{P}_{com} = [0 \quad 0 \quad h^*]^T$ in Fig. 1. The stiffness at the compliance center is expressed as follows:

$$\mathbf{K} = \mathrm{diag}([K_x \quad K_y \quad K_z \quad K_\phi \quad K_\theta \quad K_\psi]) \quad (8)$$

The tensegrity joint's motion can be described by $\mathbf{d} = \mathbf{K}^{-1} \mathbf{W}$, where $\mathbf{W}$ is the wrench applied to the compliance center. A pure force along a certain direction of the tensegrity joints at the compliance center will only produce a pure displacement, and a pure torque about the compliance center will give rise to a pure rotation. A pure torque applied at another position will produce mixed motion with rotation and translation. When a pure torque is applied on the tensegrity joint to produce small deformation, the compliance center is approximately the virtual rotational center, at which there are no translations. The following stiffness anisotropy design guarantees that the compliance center is still approximately the virtual rotational center even when arbitrary force and torque are applied on the tensegrity joint. It has been confirmed in Ref. [16] based on the stiffness matrix.

Please note that the compliance center can be designed by using Eq. (7). The tensegrity joint can achieve precise rotation around a designed rotational center. It is valuable for the tensegrity joints in robotic applications. In addition, the tensegrity joint also can be locally decoupled to design a planar joint. For example, the stiffness of directions (y, z, and ϕ) can be decoupled if $K_{y\phi} = 0$.

3.3 Stiffness Anisotropy Design. First, we introduce how to calculate the homogeneous stiffness using Eq. (8). The homogeneous stiffness can be written as a vector:

$$\begin{aligned} \mathbf{k} &= [k_x \quad k_y \quad k_z \quad k_\phi \quad k_\theta \quad k_\psi] \\ &= [K_x H^2 \quad K_y H^2 \quad K_z H^2 \quad K_\phi \quad K_\theta \quad K_\psi] \end{aligned} \quad (9)$$

where H in this article (the height of the tensegrity joint in Fig. 1) is chosen as the characteristic length and used to normalize the translational stiffness for the rotational stiffness's homogeneity [34].

A stiffness anisotropy index ξ_{mn} is proposed to measure the differences of stiffness between the DOFs quantitatively. Multiple rotational joints (revolute, universal, and ball joint) can be obtained after achieving corresponding stiffness anisotropy design with the help of the index. In detail, the stiffness of the desired rotational DOFs would be minimized, and other directions' stiffness would be maximized to get the desired rotational joint. Thus, an optimal design problem can be formulated by

$$\text{Maximizing} \quad \xi_{mn} = k_m / k_n \quad (10)$$

where k_n represents the maximum homogeneous stiffness of the desired rotational DOFs, which are selected according to the type of the desired rotational joint, and k_m represents the minimum homogeneous stiffness of other directions.

Case 1: If the tensegrity joint is designed to be a revolute joint, the desired DOF is one of ϕ, θ, and ψ. For example, if the desired DOF is ϕ, $k_m = \min(k_x, k_y, k_z, k_\theta, k_\psi)$ and $k_n = k_\phi$.

Case 2: If the tensegrity joint is designed to be a universal joint, the desired DOFs are two of ϕ, θ, and ψ. For example, if the desired DOFs are ϕ and θ, $k_m = \min(k_x, k_y, k_z, k_\psi)$ and $k_n = \max(k_\phi, k_\theta)$.

Case 3: If the tensegrity joint is designed to be a ball joint, the desired DOFs are ϕ, θ, and ψ. $k_m = \min(k_x, k_y, k_z)$ and $k_n = \max(k_\phi, k_\theta, k_\psi)$.

If $\xi_{mn} > \xi_{min}$, a minimum value, it is successful in designing the desired DOFs. This minimum value influences the axis drift mentioned in the next section, and the requirements of the axis drift should determine it. The stiffness anisotropy indexes can be listed in a vector,

$$\boldsymbol{\xi} = [\xi_{xn} \quad \xi_{yn} \quad \xi_{zn} \quad \xi_{\phi n} \quad \xi_{\theta n} \quad \xi_{\psi n}] \quad (11)$$

which is convenient to show the stiffness differences between the DOFs quantitatively.

The tensegrity joint has the desired rotational DOF after the stiffness anisotropy design, and other directions' motion are restricted by high stiffness. Next, we will explain the joint equivalence of the tensegrity joint.

3.4 Joint Equivalence. The compliance center is approximately the virtual rotational center when the tensegrity joint produces small deformation. However, for large deformation of the tensegrity joint, its stiffness matrix changes a lot. There exists a deviation between the actual rotation center and the compliance center. The deviation can be used to reflect the joint equivalence of the tensegrity joint.

To describe the deviation, we define the nominal rotational center $\mathbf{P}_{nrc}$ fixed to the follower, while the rotational center at the neutral pose $\mathbf{P}_{nrc}^0$ locates at the compliance center $\mathbf{P}_{com}$. The coordinate of the nominal rotational center at the base frame B: O–XYZ changes with the follower's rotations, as shown in Fig. 2.

The axis drift was presented to describe the joint equivalence of the tensegrity joints using the nominal rotational center, and it can be written as follows:

$$\delta = |\mathbf{P}_{nrc} - \mathbf{P}_{nrc}^0| \quad (12)$$

The axis drift is related to the size of the tensegrity joint. The dimensionless axis drift is proposed as a normalized evaluating index using the characteristic length H:

$$\delta^* = \delta / H \quad (13)$$

The axis drift in Eq. (12) is the distance between the nominal rotational centers before and after rotation: $\mathbf{P}_{nrc}$ and $\mathbf{P}_{nrc}^0$. When this distance is zero, it is believed that the rotation center of the proposed tensegrity joint does not move during motion. In other words, the joint has an accurate rotation around a fixed point and is approximately equivalent to a rigid joint. It may be difficult to achieve zero
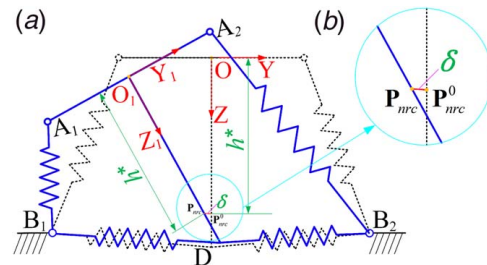

Fig. 2 Schematic of axis drift: (a) the entire structure's view and (b) its enlarged view of the partial structure. The follower frame M: $O_1 - X_1 Y_1 Z_1$ and the base frame B: O–XYZ are fixed to the follower and base, respectively. $\mathbf{P}_{nrc}^0$ is the nominal rotational center at the neutral pose, and $\mathbf{P}_{nrc}$ is the nominal rotational center after a rotation at the base frame.

axis drift all the time during a large motion for the tensegrity joint. We assume that the tensegrity joint still has an excellent joint equivalence when the dimensionless axis drift is less than 5% while the threshold of 5% is roughly obtained according to the related observation data of axis drift for flexure hinge [26,27]. The smaller the axis drift is, the better the joint equivalence is. Please note that such axis drift is not precisely equal to the deviation between the actual rotation center and the compliance center but has the same order of magnitude of the deviation. The axis drift still enables describing the joint equivalence. Its definition refers to the article [26,27].

Low axis drift is significant to achieve precise joint-like kinematics for our rotational joint. The axis drift mainly results from the coupling stiffness when the tensegrity joint is away from the neutral pose. It can be numerically calculated in the design process with static and dynamic analysis of tensegrity structures [35,36]. The tensegrity joint with low axis drift can be obtained by optimizing kinematic parameters and stiffness configurations.

3.5 Design Procedure.
The aforementioned design principle and design criterion provide a solid foundation for the tensegrity rotational joint's design. Here, the design procedure is detailed.

Each cable in the tensegrity joint is characterized by nine parameters: the stiffness k_i, elastic force τ_i, length l_i, the vectors $\mathbf{s}_{ni}$, and $\mathbf{r}_i$.

For the joint in Fig. 1, the cables in the bottom and top groups can be generated from the 1st cable and nth cable using the reflective and rotational symmetry operations, respectively. Thus, the tensegrity joint can be fully defined by an 18×1 parameter vector $\mathbf{p}$. The key is to obtain the suitable parameter vector $\mathbf{p}$ during the design of a tensegrity joint. The parameter vector $\mathbf{p}$ is obtained in three steps:

Step 1: Express the design requirements as follows:

(a) Determine the type of the desired rotational joints (revolute, universal, and ball joint) and decide the desired rotational DOFs.
(b) Give a minimum stiffness anisotropy index ξ_{min}.
(c) Give a prescribed range of axis drift. The default range is from 0% to 5%
(d) Give a targeted value $\mathbf{P}_T$ of the virtual rotational center.

Step 2: Give the initial parameters:

(a) Give a characteristic length. The default is the height of the tensegrity joint.
(b) Choose the number n of cables and plan corresponding reflective and rotational symmetry operations.
(c) Give initial parameter vector about cables written as $\mathbf{p}_0$.

Step 3: The design problem is formulated:

$$\begin{aligned} \delta^*(\mathbf{p}) &< 5\% \\ \mathbf{P}_{com}(\mathbf{p}) &= \mathbf{P}_T \\ \xi_{mn}(\mathbf{p}) &> \xi_{\min} \end{aligned} \quad (14)$$

whose constraint conditions are expressed as follows:

(a) The stiffness k_i, elastic force τ_i, and length l_i of the ith cable are positive, and $i = 1, 2, \ldots, n$.
(b) The tensegrity joint is in static balance.

The parameter vector $\mathbf{p}$ can be obtained by solving the aforementioned nonlinear inequation. There are many well-known iterative numerical methods to solve it, such as Levenberg–Marquardt algorithm.

The aforementioned design method is a simplified version for easy understanding. The design requirements and constraints can be added according to the practical application requirements. For example, the virtual rotational center can be designed in a prescribed range rather than a targeted value using Eq. (7). If the requirements of the axial drift need to be satisfied in dynamic motion, the tensegrity joint needs dynamic analysis [36].
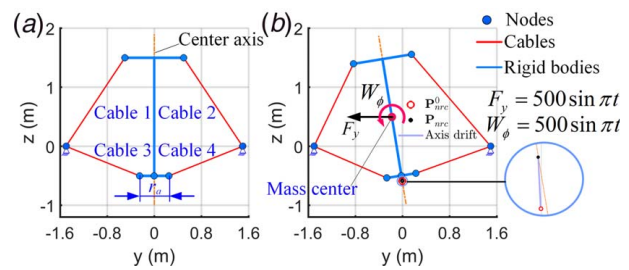
Fig. 3 (a) Structure of tensegrity joints and (b) a joint's rotational pose with a small axis drift

The method also can design an active tensegrity joint. In this case, the active tension elements provide workload to deform the tensegrity joint rather than adopting an external load. Please note that there will be one more design requirement due to the different loading methods: the active tension elements' parameter variations due to actuation should be considered in the joint equivalence design.

The design method focuses on three key steps: calculating the compliance center, stiffness anisotropy design, and joint equivalence analysis. There are no strict requirements of the cable arrangement for the three steps. These steps can be done with symmetrically arranged cables or with individually designed cables. The former design is simpler and can be solved faster because of fewer design parameters. It is the main reason to emphasize the design in this article. If necessary, all the cables can also be individually designed to find the required joint.

In addition, please note other tensegrity joints, which has appeared in the emerging bio-tensegrity models [7,17,19], manipulators [21,22], and robotics [23]. These tensegrity joints can also be designed by the proposed method and achieve precise joint-like motions by analyzing their joint equivalence.

3.6 Numerical Examples.
Two successful planar tensegrity rotational joints, cases 1 and 2, are exemplified to elaborate on the joint equivalence. They have different virtual rotational centers and axis drifts, which are only caused by two different parameters. In Fig. 3(a), the radius of platform r_a is 0.25 m for case 1 and is 0.75 m for case 2. The pretension of cable 3 and 4 is about 112.02 N for case 1 and is 75 N for case 2. Their other structural parameters are the same in Fig. 3(a). The stiffness and pretension of cables 1 and 2 are 1e3 N/m and 50 N, respectively. The stiffness of cables 3 and 4 are 1e5 N/m. The damping coefficient of all the cables is 20 Ns/m.

We focused on the stiffness of DOFs (y, z, and ϕ) for the planar tensegrity joints. The stiffness indexes of DOFs (y and z) with respect to DOF ϕ are calculated using Eqs. (3) and (11). For case 1, the vector of the index is $\boldsymbol{\xi} \approx [138 \quad 23 \quad 1]$. For case 2, the vector of the index is $\boldsymbol{\xi} \approx [83 \quad 37 \quad 1]$.

Tensegrity joints are simulated under the external torque $W_\phi = 500 \sin \pi t$ and external force $F_y = 500 \sin \pi t$. As shown in Fig. 3(b), the external torque and force are applied to the rigid body's mass center. Figure 3(b) also shows a joint's rotational pose with a small axis drift, which is the distance between the nominal rotational centers $\mathbf{P}_{nrc}^0$ and $\mathbf{P}_{nrc}$ before and after rotation.

Figures 4(a) and 4(b) show the rotations of case 1 under the external torque and external force, respectively. Similarly, Figs. 4(c) and 4(d) show the rotations of case 2 under the external torque and force, respectively. The dynamic rotations also can be seen in movies 1–4.[2] For each case, the actual rotational center, which is the intersection point of all the center axes of the platforms, is nearly located at the corresponding compliance center $\mathbf{P}_{nrc}^0 = [0 \quad 0 \quad h^*]^T$ in Fig. 4. The two cases' virtual rotational centers

---

[2]The movies are available on Youtube: https://youtu.be/ba5V7Ex7Tbk
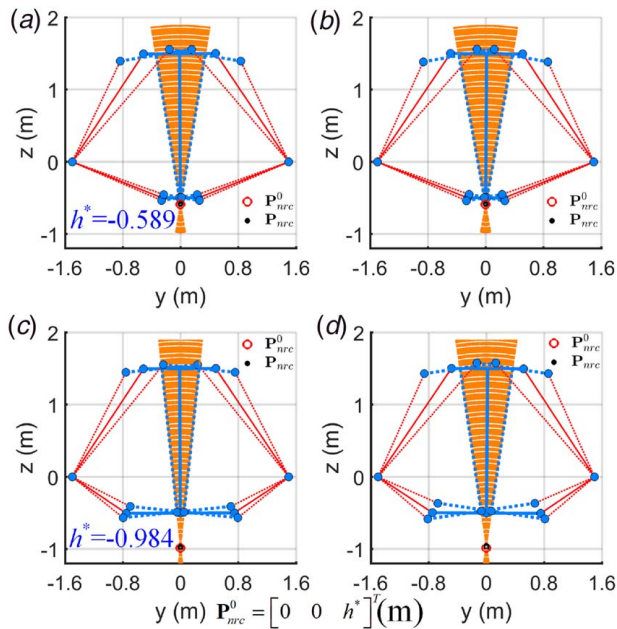
Fig. 5 Axis drifts: (a) case 1 and (b) case 2

Fig. 4 Rotations. (a) and (b) Case 1 and (c) and (d) case 2. (a) and (c) The rotations under the external torque W_ϕ. (b) and (d) The rotations under the external force F_y. In each figure, three rotational poses are plotted in dotted lines to help show the joint's rotations. The center axes of all the poses are plotted to observe the rotational centers.

are entirely different and can be designed using Eq. (7). The ability to design the tensegrity joint's rotational center is unique. It provides the capacity to adjust its rotational center at any time just by changing structural parameters and elastic forces of cables. It may provide new insight into making robots.

The axis drifts of the two cases are shown in Fig. 5. The maximum axis drift for case 1 is about 7.8 mm, and the corresponding dimensionless axis drift is 0.39%, while the height H of the tensegrity joint is the characteristic length and is 2 m. The maximum axis drift for case 2 is about 31.6 mm, and the corresponding dimensionless axis drift is 1.58%. The axis drifts show their excellent joint equivalence, especially the ones of case 1.

The conventional rigid joints can be assembled into a serial structure, such as a robotic arm. The proposed compliant tensegrity joint with excellent joint equivalence also can be a modular joint to construct a serial structure. A serial structure is exemplified in Fig. 6 and comprises two tensegrity joints (case 2). Figure 6 shows its three rotational poses under the external torque W_ϕ applied on the second joint. Its dynamic rotations also can be seen in movie 5[3]. We can observe that the rotations of the two joints are around their corresponding compliance centers. The second joint's rotation is relative rotation with respect to the first joint.

One successful universal joint with rotational DOFs θ and ψ is also exemplified. Its structural parameters are shown in Fig. 7. The stiffness and pretension of cables 1–2 are about 1e4 N/m and 200 N, respectively. The stiffness and pretension of cable 3–6 are about 1e5 N/m and 150 N, respectively. The damping coefficient of all the cables is 20 Ns/m. The vector of the stiffness index for the universal joint is $\xi \approx [263 \quad 806 \quad 517 \quad 62 \quad 1 \quad 0.86]$.

The joint is simulated under the external force $F_x = 200 \sin 4\pi t$ along the x-direction, the external torque $W_\psi = 500 \sin 4\pi t$ along the ψ-axis, and the combined force of F_x and W_ψ. As shown in Fig. 7(b), the external torque and force are applied to the rigid body's mass center.

Figures 8–10 show the universal joint's rotations under the external load. For each simulation, the actual rotational center, which is
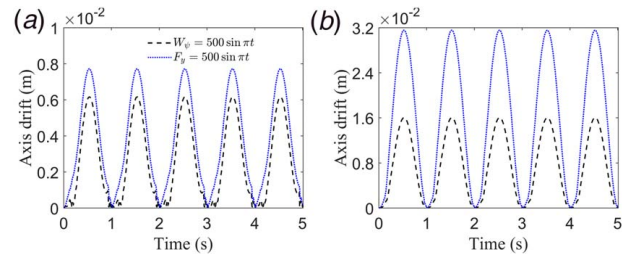
the intersection point of all the center axes of the platforms, is nearly located at the corresponding compliance center $\mathbf{P}^0_{nrc} = [0 \quad 0 \quad -0.9936]^T$ m. The maximum axis drift is about 50 mm in Fig. 10(c), and the corresponding dimensionless axis drift is 2.5%. The axis drifts show excellent joint equivalence.

4 Experiments

Two experiments will be introduced. In the first experiment, a tensegrity joint is developed to verify the joint equivalence and the feasibility of a large-size joint experimentally. The second experiment demonstrates a modular application of tensegrity joints assembled into a robotic arm.

4.1 Experiments of Joint Equivalence. The experiment setup of the rotational tensegrity joint is shown in Fig. 11. We focus on the tensegrity joint's joint equivalence and measure its axis drifts at different poses.

The pneumatic muscles (Festo DMSP-5) as active tension elements are used to actuate the tensegrity joint to reach different poses with the help of proportional pressure valves (Festo VPPM-6L) and force sensors (ZNLBM-300N). The cables as passive tension elements provide a passive tension network to support the follower in suspension. They are not directly actuated and deform to distribute the external load throughout the entire structure.

The tensegrity joint's poses were measured by pose measurement techniques of monocular vision using an MV-1000U3C camera (ten million pixels) and markers, as shown in Fig. 11. At the neutral pose, the nominal length, contraction ratio, and inflation pressure of pneumatic muscles are 341 mm, 7.5%, and 5 bar, respectively. The length of support bars of the follower is 620 mm.

According to the design method, the tensegrity joint has been designed to be a 3-DOF (ϕ, θ, and ψ) rotational joint. Since the design focuses on the passive properties, cables' stiffness is considered without regard to the pneumatic muscles for convenience. Its structural parameters are listed in Table 1, while the structural parameter definitions are shown in Fig. 1. At the base frame, the compliance center is $\mathbf{P}_{com} = [0 \quad 0 \quad 407.8]^T$ mm. According to these parameters, the stiffness index of each DOF is calculated with the help of Eq. (10), while the DOF (ψ) has the maximum rotational stiffness, about 470 Nm/rad in DOFs (ϕ, θ, and ψ). They can be listed in a vector $\xi \approx [4.13e8 \quad 4.13e8 \quad 6.24e6 \quad 0.51 \quad 0.51 \quad 1]$ corresponding to the stiffness matrix in Eq. (11).

The tensegrity joint reached different poses of rotational DOF (ϕ, θ, and ψ) actuated by active tension elements. Some poses among them are shown in Fig. 12. The axis drift and dimensionless axis drift are calculated by these poses with the help of Eqs. (12) and (13).

Figure 13 shows that the relationship among rotation angles (0–5°), axis drifts, and dimensionless axis drifts. The maximum axis drift is about 7.5 mm. The maximum dimensionless axis drift is less than 2%. The data are acceptable and less than the prescribed maximum value of 5% so that the joint equivalence of the tensegrity joint is validated.

[3]The movie is available on Youtube: https://youtu.be/ba5V7Ex7Tbk

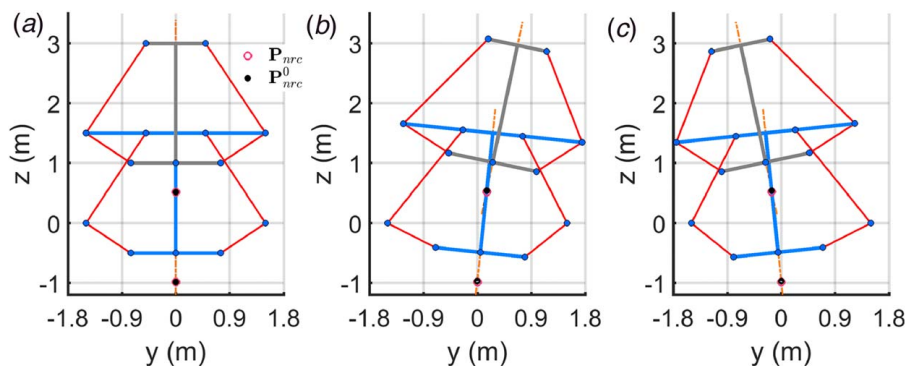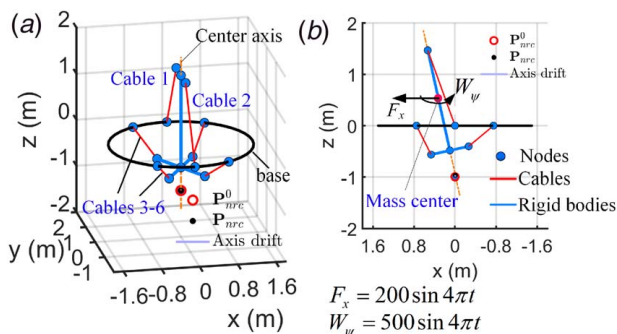Fig. 6 The rotations of a serial structure

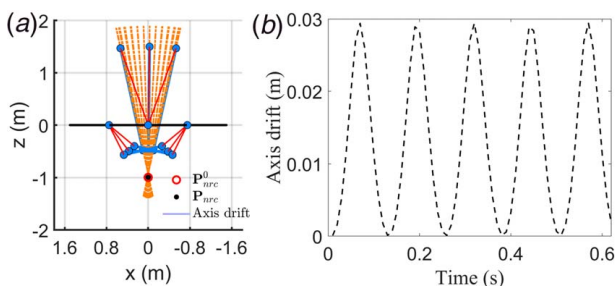Fig. 7 (a) A universal joint with six cables and (b) a joint's rotational pose in the x–z plane

Fig. 8 Rotations of the joint under the external torque F_x: (a) front view in the x–z plane and (b) axis drift. In (a), three rotational poses are plotted in dotted lines to help show the joint's rotations. The center axes of all the poses are plotted to observe the rotational centers.

Fig. 9 Rotations of the joint under the external torque W_ψ: (a) top view in the x–y plane and (b) axis drift

Fig. 10 Rotations of the joint under the external force W_ψ and force F_x: (a) front view in the x–z plane, (b) top view in the x–y plane, (c) three-dimensional view, and (d) axis drift

4.2 Experiments of Tensegrity Robotic Arms. The modular nature of the tensegrity mechanism has been demonstrated [37–39]. Similarly, the proposed compliant tensegrity joints can replace rigid joints as modular joints to construct a hyper redundant serial structure. For example, a large-size robotic arm can be developed by assembling large-size tensegrity joints illustrated in Fig. 11. Since it is difficult to build because of the size effects and high cost, a small-size robotic arm is developed in Fig. 14 to verify the feasibility. The robotic arm comprises 17 passive tensegrity joints fabricated with ABS material by the 3D printer, and its length is 741 mm. Each joint in Fig. 14(c) comprises two platforms and five springs divided into two groups: the horizontal group like spring 1 and the vertical group like spring 2. The tensegrity joint in Fig. 14 is a variant of the joint in Fig. 1 by using the vertical spring to replace the joint's top cable network. Each joint's compliance center is located at the center of horizontal groups. The structural parameters are detailed in Figs. 14(d)–14(f).
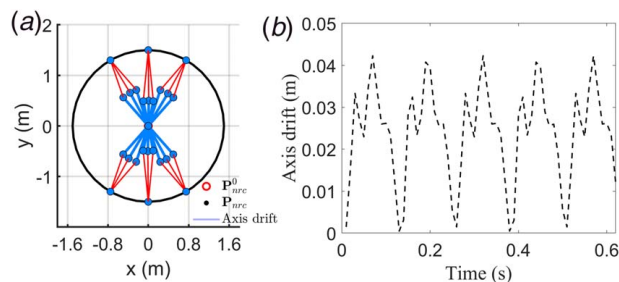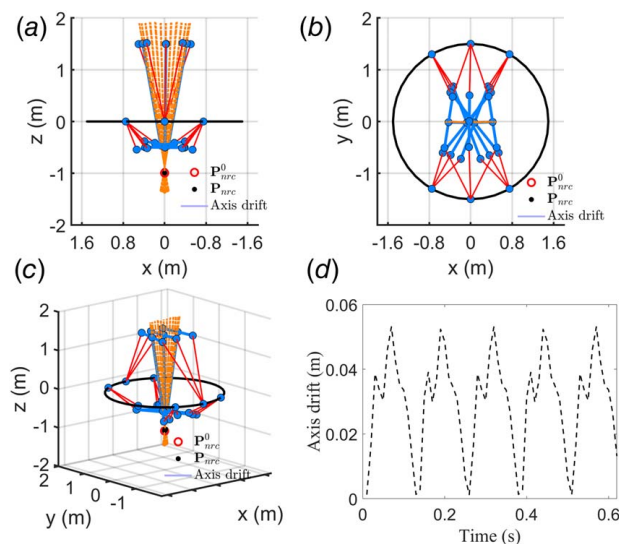
There are four actuation cables in Fig. 14(f) attached to the tensegrity robotic arm. Figure 14(b) shows its actuation system, including four motors with encoders, eight pulleys, a microcontroller, and a battery. By adjusting their length using motors, four bending shapes are shown in Fig. 15. In Fig. 14(f), the combination of HL and VL fixed to the joint's platforms is used to observe the curvature and joints" rotations easily. Figure 15 shows the bending deformations of the tensegrity arms with the auxiliary lines. The relative rotation of each tensegrity joint forms smooth variations of the curvature. Figure 15(e) shows the magnifying view to observe the joints' actual rotational centers, approximately the adjacent VLs" intersection points. In Fig. 15(f), most actual rotational
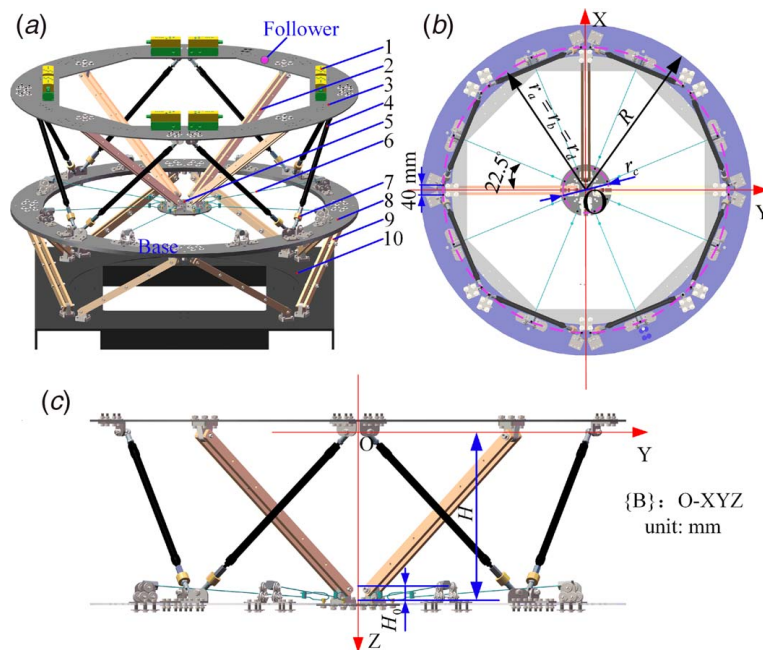
Fig. 11 Experiment setup. (*a*) Three-dimensional view. (*b*) Top view of the tensegrity joint. The base is recolored, and the plate is transparent to show the dimensions clearly. (c) Front view of the tensegrity joint. This experiment platform is a two-layer structure. The bottom layer is a fixed parallel mechanism to support the top layer, i.e., the tensegrity joint. There are many components: (1) proportional pressure valve, (2) support bars of the follower, (3) follower plate of tensegrity joint, (4) pneumatic muscles, (5) follower's foot, (6) cables, (7) force sensor, (8) base of tensegrity joint, (9) fixed bars of the base, and (10) foundation. The follower's mass is about 38.9 kg, and its center of mass is about [0 0 55] mm at the base frame B.

Table 1 Parameters of tensegrity joint

| Definition	Notation	Value (mm)
Outer radius of the follower and base	R	640
Radius of lower joint points of pneumatic muscles	r_a	550
Radius of upper joint points of pneumatic muscles	r_b	550
Radius of upper joint points of cables on the follower's plate	r_c	90
Radius of lower joint points of cables on the base	r_d	550
Height of follower	H	400
Height between upper and lower joint points of cables	H_0	40
Diameter of cables	d	1
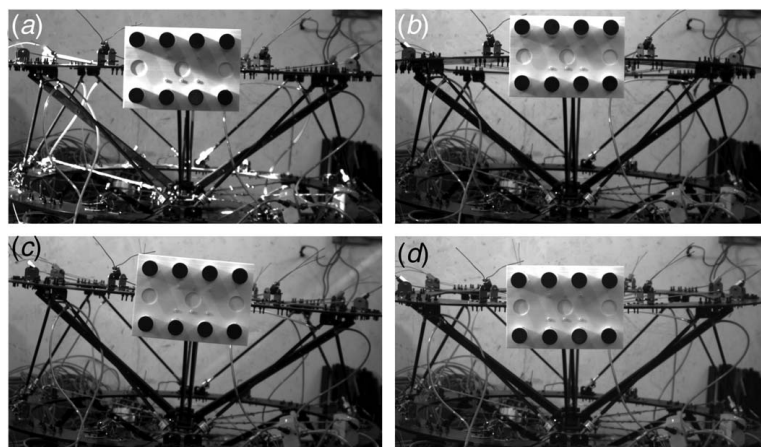
Fig. 12 Different poses of the tensegrity joint. (*a*) the neutral pose, (*b*) the anticlockwise rotation about DOF θ, (c) the clockwise rotation about DOF ϕ, and (*d*) the clockwise rotation about DOF θ
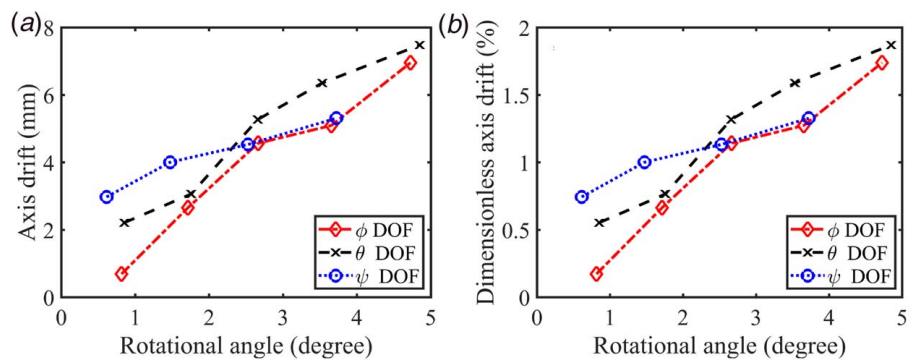
Fig. 13 Axis drifts with different rotational angles: (*a*) axis drifts and (*b*) dimensionless axis drifts
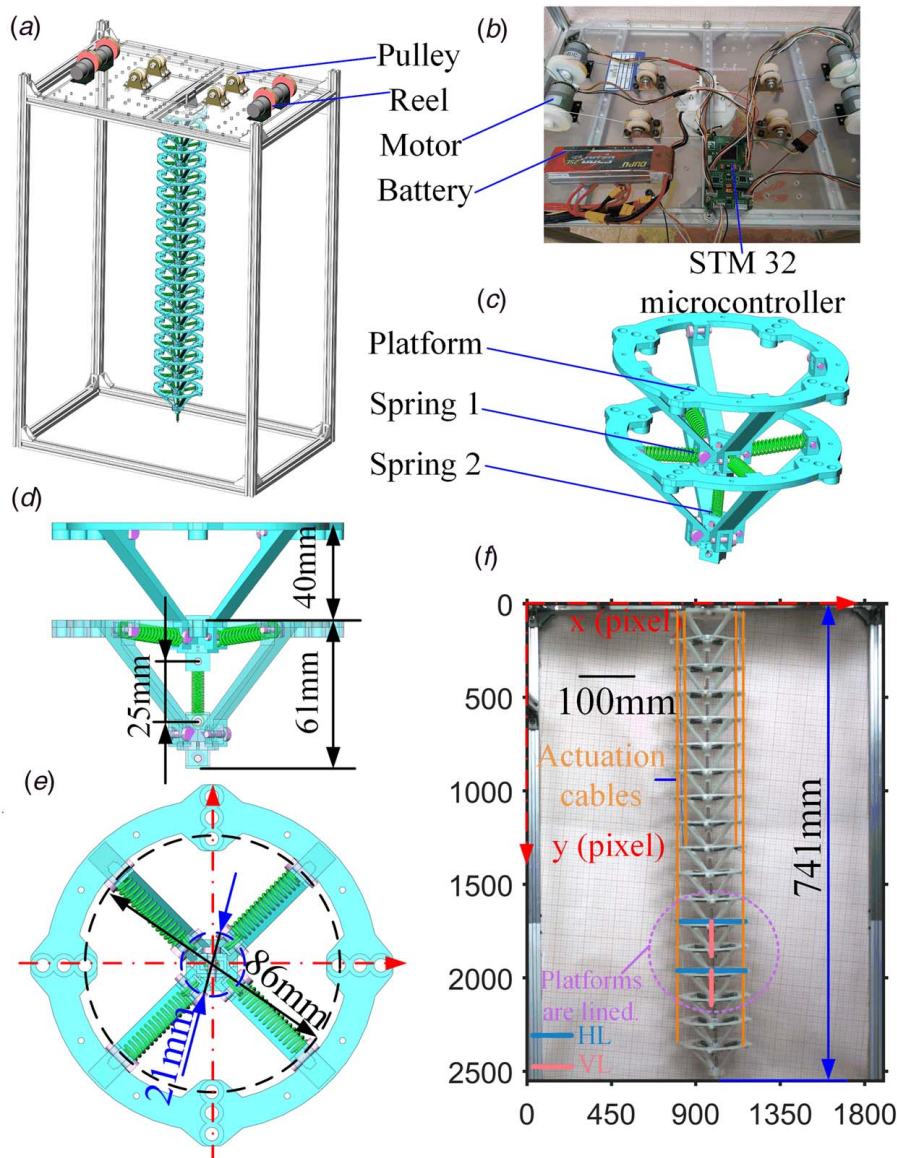

Fig. 14 The schematic of the experimental platform. (*a*) The overall structure. (*b*) The actuation system comprises motors, electrical components including a microcontroller and a battery, and a mechanical transmission system including pulleys and reels. A tensegrity joint in (*c*) comprises two platforms and five springs. The rest length, diameter, and coil diameter of spring 1 are 30, 6, and 0.8 mm, respectively. The rest length, diameter, and coil diameter of spring 2 are 15, 5, and 0.5 mm, respectively. (*d*) and (*e*) The platform's structural parameters. (*f*) The tensegrity robotic arm. Quadrille paper was used as the background, and the coordinates are defined by pixels. HL, horizontal line; VL, vertical line. They are used to represent the platform.
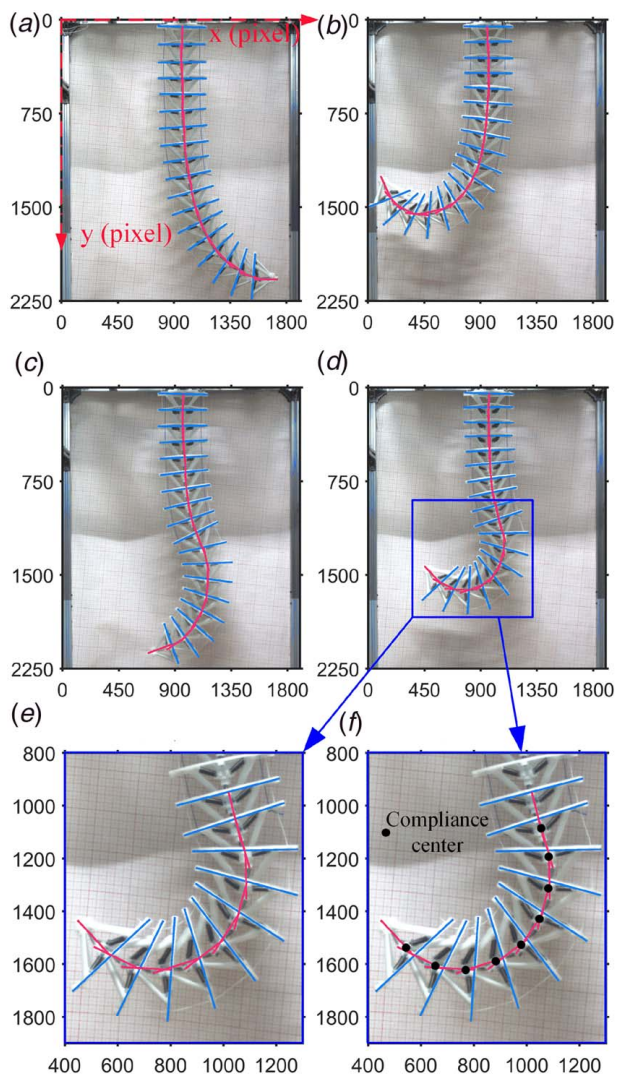
Fig. 15 Bending deformations. (*a*) and (*b*) Two C-shape bending deformations. (*c*) and (*d*) Two S-shape bending deformations. (*e*) A part of (*d*) and is magnified to show the joints' rotation clearly. (*f*) The image is reproduced from (*e*) and marks out the compliance center of each tensegrity joint.

centers are almost located at the tensegrity joints' compliance centers, especially for the joint with small rotation. The tensegrity joints still can achieve excellent joint equivalence when as modular joints in a serial structure. The result has been reflected in Fig. 6(*f*). In summary, the experiment demonstrates the proposed compliant tensegrity joints' ability to replace rigid joints as modular joints to construct a serial structure. It is the important application of the proposed tensegrity joints.

5 Discussion

We demonstrated low axis drifts of small rotation angles (0–5°) for the large-size tensegrity joint in Fig. 11. Small rotational angles are caused by the passive tension network's large stiffness since the elastic deformation is generally inversely proportional to the stiffness.

Through the numerical calculations of static equilibrium equations, we demonstrated the variation of rotational angle range by varying the stiffness of the passive tension network for the joint in Fig. 16. The range of rotational angle increased by decreasing stiffness of the passive tension network. In fact, the tensegrity joint in Fig. 11 is developed to construct a large-size tensegrity robotic fish for future study and works in a small range, about rotation angle of 0–2 deg [16]. Based on the study's starting point, the joint is restricted in a small range of motion. The range of motion for the tensegrity robotic fish would be mainly determined by the number of joints. Of course, the range of motion for a single joint is also significant. The tensegrity joint can have a wide range of rotations by optimizing its structural parameters. For example, the simulated planar tensegrity joint in Fig. 4 has rotations of about -10 to 10 deg.

The relationship between the axis drifts and the stiffness of the passive tension network is complicated. The axis drifts of the maximum rotational angle may increase or decrease by decreasing the passive tension network's stiffness. This complicated relationship may be related to joint kinematic parameters. In the future, exploring the joints' nonlinear deformation characteristics can uncover more systematic design theory, improve the precision of joint-like kinematics, and optimize the workspace. More interesting characteristics and works of the proposed tensegrity rotational joints can be explored by learning from the flexure hinges [25,27,26] and other compliant joints [40]. For example, the method to design a compliant joint with a prescribed wrench-feasible workspace can be referred to Ref. [40]. In addition, please note that there exists a minor difference between the experimental results and simulation
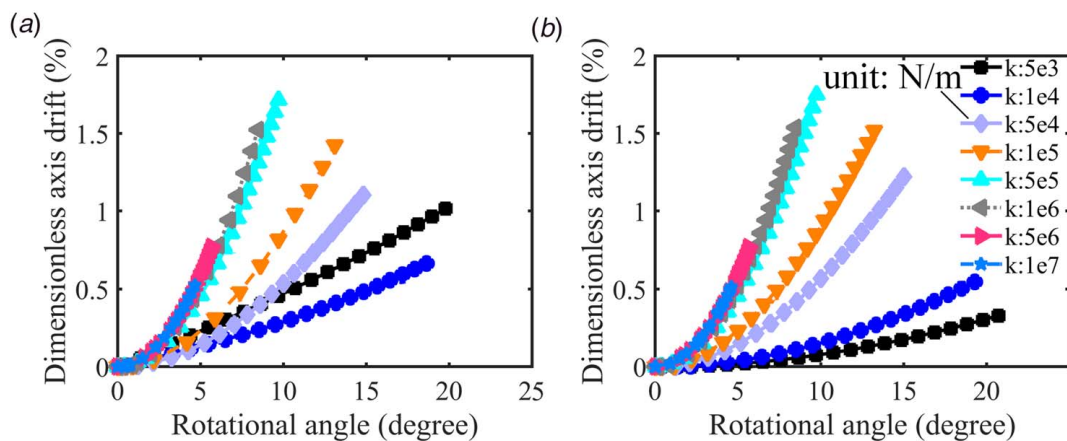

Fig. 16 Dimensionless axis drifts of static response by varying stiffness of passive tension network. (*a*) Axis drifts under external force. (*b*) Axis drifts under external torque. The force is along the direction of DOF (*x*), and its range is 0–100N. The torque is along the direction of DOF (*θ*), and its range is 0–40 Nm. The external load is applied to the plate's center and would cause different rotational angles (absolute values) of DOF (*θ*) for the follower.

results. The difference might mainly result from the compound influences of the platform mass and assembly errors.

Our tensegrity joint used its elastic deformation to transfer motion, force, and energy. We emphasized its design aspect, and the tensegrity joint can achieve precise rigid joint-like kinematics, that is, excellent joint equivalence. High-precise rigid body joints can achieve precise joint-like motion. They need to use conventional bearings due to the need for lubrication and are difficult to work inside a vacuum, wet, or dirty environment [26]. It is also challenging to make a large-size rigid joint. The tensegrity joint can be used at different scales and sizes and has a great potential to work inside the unstructured environment.

Currently, we only adopted the axis drift reflecting the drift of the center of rotation. In fact, a rotational axis is defined by not only a rotational center but also its direction. There may exist the noncollineation between the actual axis of rotation and the desired rotational axis in the actual application. The noncollineation may result from assembly errors, the internal force of cables, and the external environment. The noncollinear index can be formulated by the directional cosine of the two axes and can be restricted through stiffness anisotropy design. In the future, the index can be considered in the design of the tensegrity joint.

Furthermore, the tensegrity joints contribute many notable benefits, such as high mechanical efficiency, bio-inspired, lightweight, adaptability of environment, modularity, and scalability. These significant structural characteristics provide great potential for our tensegrity joints to extend in many robotic applications for unstructured environments. For example, a large-size robotic fish (like a blue whale) can be developed based on our previous works [16] and swim freely in the ocean assembled by many tensegrity joints in Fig. 11. Moreover, large-size robotic arms assembled by modular tensegrity joints can be expected in precise operation at sea or space, with learning algorithms or artificial intelligence. These imaginations can be achieved with a high probability since we have demonstrated the tensegrity joints' modularity characteristic using a tensegrity robotic arm.

In addition, the tensegrity joint's design helps control hyper redundant serial structures constructed by tensegrity joints. The tensegrity joint can achieve accurate rotation around the designed rotational center, and thus, its translation can be represented by the rotations. It is valuable for the kinematic analysis and control of hyper redundant serial structures. The tensegrity robotic arm in Fig. 15 can demonstrate its high flexibility and express plenty of bending deformations after complementing the complicated shape control.

6 Conclusions

In this study, we presented a method to design the tensegrity rotational joint, which makes its elastic deformation under an external force and torque to become an accurate rotation around the compliance center, that is, its virtual rotational center. Such tensegrity joint can achieve precise rigid joint-like kinematics around specific rotational centers through designing the compliance center and replace rigid joints to transfer motion, force, and energy.

Hence, the stiffness matrix of the tensegrity joints was formulated and decoupled to design each DOF's stiffness independently. The compliance center was derived. The stiffness anisotropy index was proposed to complete stiffness anisotropy design according to the relationship between the stiffness anisotropy and DOFs. The axis drift and its dimensionless one were presented as an evaluation index to describe quantitatively joint equivalence. Axis drift in a prescribed range of 0–5% implies that the tensegrity joint achieved a precise rotation so that this joint is equivalent to a rigid joint. The complete design process of the tensegrity joint was introduced. Numerical examples were presented to verify the effectiveness of the proposed design method. Two planar tensegrity rotational joints, a universal joint, and a serial structure constructed by tensegrity joints were exemplified to show the rotations around their compliance centers and elaborate on the joint equivalence.

A 3-DOF and large-size tensegrity joint were developed through the design method to verify the joint equivalence experimentally. Such a tensegrity joint is approximately equivalent to a rigid ball joint. Its external diameter is 1.28 m, and its height is 0.4 m. Experimental results showed that the tensegrity joint can achieve low dimensionless axis drifts of less than 2%, and indicated its excellent joint equivalence. The feasibility of a large-size joint is verified experimentally. A robotic arm constructed by 17 tensegrity joints was developed to demonstrate the proposed joints' modularity characteristic. In a serial structure, each tensegrity joint's relative rotations can form smooth curvature variation.

Due to structural benefits as a tensegrity structure, achieved large-size attempt, and excellent joint equivalence, the proposed tensegrity rotational joint can extend in many robotic applications at different scales and sizes.

Acknowledgment

Conflict of Interest

There are no conflicts of interest.

Data Availability Statement

The datasets generated and supporting the findings of this article are obtainable from the corresponding author upon reasonable request. The authors attest that all data for this study are included in the paper.

References

[1] Skelton, R., and de Oliveira, M., 2009, *Tensegrity Systems*, Springer, New York.
[2] Sultan, C., 2009, "Tensegrity: 60 Years of Art, Science, and Engineering," *Advances in Applied Mechanics*, Elsevier, Vol. 43, pp. 69–145.
[3] Motro, R., 2003, *Tensegrity: Structural Systems for the Future*, Kogan Page Science, London.
[4] Ingber, D., 2003, "Tensegrity I. Cell Structure and Hierarchical Systems Biology," J. Cell Sci., **116**(7), pp. 1157–1173.
[5] Rhode-Barbarigos, L., Ali, N. B. H., Motro, R., and Smith, I., 2010, "Designing Tensegrity Modules for Pedestrian Bridges," Eng. Struct., **32**(4), pp. 1158–1167.
[6] Pellegrino, S., 1992, "A Class of Tensegrity Domes," Int. J. Space Struct., **7**(2), pp. 127–142.
[7] Scarr, G., 2010, "Simple Geometry in Complex Organisms," J. Bodyw. Mov. Ther., **14**(4), pp. 424–444.
[8] Snelson, K., 2012, "The Art of Tensegrity," Int. J. Space Struct., **27**(2–3), pp. 71–80.
[9] Paul, C., Valero-Cuevas, F. J., and Lipson, H., 2006, "Design and Control of Tensegrity Robots for Locomotion," IEEE Trans. Robot., **22**(5), pp. 944–957.
[10] Sun, J., Song, G., Chu, J., and Ren, L., 2019, "An Adaptive Bioinspired Foot Mechanism Based on Tensegrity Structures," Soft Robot., **6**(6), p. soro.2018.0168.
[11] Orki, O., Ayali, A., Shai, O., and Ben-Hanan, U., 2012, "Modeling of Caterpillar Crawl Using Novel Tensegrity Structures," Bioinspir. Biomim., **7**(4), p. 046006.
[12] Koizumi, Y., Shibata, M., and Hirai, S., 2012, "Rolling Tensegrity Driven by Pneumatic Soft Actuators," IEEE International Conference on Robotics and Automation, Saint Paul, MN, May 14–18, pp. 1988–1993.
[13] Sabelhaus, A. P., Bruce, J., Caluwaerts, K., Manovi, P., Firoozi, R. F., Dobi, S., Agogino, A. M., and SunSpiral, V., 2015, "System Design and Locomotion of Superball, an Untethered Tensegrity Robot," IEEE International Conference on Robotics and Automation, Seattle, WA, May 26–30, pp. 2867–2873.
[14] Friesen, J., Pogue, A., Bewley, T., de Oliveira, M., and Sunspiral, V., 2014, "Ductt: A Tensegrity Robot for Exploring Duct Systems," IEEE International Conference on Robotics and Automation, Hong Kong, China, 31 May-June 7.
[15] Bliss, T., Iwasaki, T., and Bart-Smith, H., 2012, "Central Pattern Generator Control of a Tensegrity Swimmer," IEEE-ASME Trans. Mechatron., **18**(2), pp. 586–597.

[16] Chen, B., and Jiang, H., 2019, "Swimming Performance of a Tensegrity Robotic Fish," Soft Robot., **6**(4), p. soro.2018.0079.

[17] Flemons, T., 2012, "The Bones of Tensegrity," http://intensiondesigns.ca/bones-of-tensegrity/, Accessed November, 2019.

[18] Levin, S. M., 1997, "Putting the Shoulder to the Wheel: A New Biomechanical Model for the Shoulder Girdle," J. Biomed. Sci. Instrum., **33**, pp. 412–417.

[19] Levin, S. M., 2002, "The Tensegrity-Truss as a Model for Spine Mechanics: Biotensegrity," J. Mech. Med. Biol., **2**(03n04), pp. 375–388.

[20] Scarr, G., and Harrison, H., 2017, "Examining the Temporo-Mandibular Joint From a Tensegrity Perspective: A Change in Thinking," J. Appl. Biomed., **15**(1), pp. 55–62.

[21] Lessard, S., Castro, D., Asper, W., Chopra, S. D., Baltaxe-Admony, L. B., Teodorescu, M., SunSpiral, V., and Agogino, A., 2016, "A Bio-Inspired Tensegrity Manipulator With Multi-dof, Structurally Compliant Joints," IEEE/RSJ International Conference on Intelligent Robots and Systems (IROS), Daejeon, South Korea, Oct. 9–14, pp. 5515–5520.

[22] Lessard, S., Bruce, J., Jung, E., Teodorescu, M., SunSpiral, V., and Agogino, A., 2016, "A Lightweight, Multi-Axis Compliant Tensegrity Joint," IEEE International Conference on Robotics and Automation, Stockholm, Sweden, May 16–21, pp. 630–635.

[23] Friesen, J. M., Dean, J. L., Bewley, T., and Sunspiral, V., 2018, "A Tensegrity-Inspired Compliant 3-dof Compliant Joint," IEEE International Conference on Robotics and Automation, Brisbane, QLD, Australia, May 21–25, pp. 3301–3306.

[24] Jung, E., Ly, V., Cessna, N., Ngo, M. L., Castro, D., SunSpiral, V., and Teodorescu, M., 2018, "Bio-Inspired Tensegrity Flexural Joints," IEEE International Conference on Robotics and Automation, Brisbane, QLD, Australia, May 21–25, pp. 5561–5566.

[25] Howell, L. L., 2013, *Compliant Mechanisms*, Springer, London.

[26] Machekposhti, D. F., Tolou, N., and Herder, J. L., 2015, "A Review on Compliant Joints and Rigid-Body Constant Velocity Universal Joints Toward the Design of Compliant Homokinetic Couplings," ASME J. Mech. Des., **137**(3), p. 032301.

[27] Yong, Y., Lu, T., and Handley, D. C., 2008, "Review of Circular Flexure Hinge Design Equations and Derivation of Empirical Formulations," Precis. Eng.-J. Int. Soc. Precis. Eng. Nanotechnol., **32**(2), pp. 63–70 .

[28] Thomas, T. L., Kalpathy Venkiteswaran, V., Ananthasuresh, G. K., and Misra, S., 2021, "Surgical Applications of Compliant Mechanisms: A Review," ASME J. Mech. Robot., **13**(2), p. 020801.

[29] Mirletz, B. T., Bhandal, P., Adams, R. D., Agogino, A. K., Quinn, R. D., and SunSpiral, V., 2015, "Goal-directed CPG-Based Control for Tensegrity Spines With Many Degrees of Freedom Traversing Irregular Terrain," Soft Rob., **2**(4), pp. 165–176.

[30] Böhm, V., Kaufhold, T., Schale, F., and Zimmermann, K., 2016, "Spherical Mobile Robot Based on a Tensegrity Structure With Curved Compressed Members," 2016 IEEE International Conference on Advanced Intelligent Mechatronics (AIM), Banff, AB, Canada, July 12–15, pp. 1509–1514.

[31] Dasgupta, B., and Mruthyunjaya, T., 2000, "The Stewart Platform Manipulator: A Review," Mech. Mach. Theory, **35**(1), pp. 15–40.

[32] Azadi, M., Behzadipour, S., and Faulkner, G., 2009, "Antagonistic Variable Stiffness Elements," Mech. Mach. Theory, **44**(9), pp. 1746–1758.

[33] Jiang, H., He, J., and Tong, Z., 2010, "Characteristics Analysis of Joint Space Inverse Mass Matrix for the Optimal Design of a 6-dof Parallel Manipulator," Mech. Mach. Theory, **45**(5), pp. 722–739.

[34] Angeles, J., 2006, "Is There a Characteristic Length of a Rigid-Body Displacement?," Mech. Mach. Theory, **41**(8), pp. 884–896.

[35] Juan, S. H., and Tur, J. M. M., 2008, "Tensegrity Frameworks: Static Analysis Review," Mech. Mach. Theory, **43**(7), pp. 859–881.

[36] Tur, J. M. M., and Juan, S. H., 2009, "Tensegrity Frameworks: Dynamic Analysis Review and Open Problems," Mech. Mach. Theory., **44**(1), pp. 1–18.

[37] Arsenault, M., and Gosselin, C., 2006, "Kinematic and Static Analysis of a Planar Modular 2-dof Tensegrity Mechanism," Proceedings 2006 IEEE International Conference on Robotics and Automation, Orlando, FL, May 15–19, pp. 4193–4198.

[38] Muralidharan, V., and Wenger, P., 2019, "Kinetostatic Analysis and Actuation Strategy of a Planar Tensegrity 2-x Manipulator," ASME J. Mech. Robot., **11**(6), p. 060904.

[39] Moored, K. W., Kemp, T., Houle, N., and Bart-Smith, H., 2011, "Analytical Predictions, Optimization, and Design of a Tensegrity-Based Artificial Pectoral Fin," Int. J. Space Struct., **48**(22–23), pp. 3142–3159.

[40] Muralidharan, V., and Wenger, P., 2021, "Optimal Design and Comparative Study of Two Antagonistically Actuated Tensegrity Joints," Mech. Mach. Theory, **159**, p. 104249.